The Astrophysical Journal, 714:1108–1119, 2010 May 10 doi:10.1088/0004-637X/714/2/1108

MEASUREMENTS OF THE CORONAL ACCELERATION REGION OF A SOLAR FLARE

Säm Krucker[1], H. S. Hudson[1], L. Glesener[1,2], S. M. White[3,4], S. Masuda[5], J.-P. Wuelser[6], and R. P. Lin[1,2,7]
[1] Space Sciences Laboratory, University of California, Berkeley, CA 94720-7450, USA; krucker@ssl.berkeley.edu
[2] Department of Physics, University of California, Berkeley, CA 94720-7300, USA
[3] Department of Astronomy, University of Maryland, College Park, MD 20742, USA
[4] Air Force Research Laboratory, Space Vehicles Directorate, Hanscom Air Force Base, MA, USA
[5] Solar–Terrestrial Environment Laboratory, Nagoya University, Furo-cho, Chikusa-ku, Nagoya, Aichi 464-8601, Japan
[6] Solar and Astrophysics Laboratory, Lockheed Martin ATC, 3251 Hanover Street, Palo Alto, CA 94304, USA
[7] School of Space Research, Kyung Hee University, Yongin, Gyeonggi 446-701, Republic of Korea
Received 2009 June 9; accepted 2010 March 18; published 2010 April 16

ABSTRACT

The *Reuven Ramaty High Energy Solar Spectroscopic Imager* (*RHESSI*) and the Nobeyama Radioheliograph (NoRH) are used to investigate coronal hard X-ray and microwave emissions in the partially disk-occulted solar flare of 2007 December 31. The *STEREO* mission provides EUV images of the flare site at different viewing angles, establishing a two-ribbon flare geometry and occultation heights of the *RHESSI* and NoRH observations of ∼16 Mm and ∼25 Mm, respectively. Despite the occultation, intense hard X-ray emission up to ∼80 keV occurs during the impulsive phase from a coronal source that is also seen in microwaves. The hard X-ray and microwave source during the impulsive phase is located ∼6 Mm above thermal flare loops seen later at the soft X-ray peak time, similar in location to the above-the-loop-top source in the Masuda flare. A single non-thermal electron population with a power-law distribution (with spectral index of ∼3.7 from ∼16 keV up to the MeV range) radiating in both bremsstrahlung and gyrosynchrotron emission can explain the observed hard X-ray and microwave spectrum, respectively. This clearly establishes the non-thermal nature of the above-the-loop-top source. The large hard X-ray intensity requires a very large number ($>5 \times 10^{35}$ above 16 keV for the derived upper limit of the ambient density of $\sim 8 \times 10^9$ cm^{-3}) of suprathermal electrons to be present in this above-the-loop-top source. This is of the same order of magnitude as the number of ambient thermal electrons. We show that collisional losses of these accelerated electrons would heat all ambient electrons to superhot temperatures (tens of keV) within seconds. Hence, the standard scenario, with hard X-rays produced by a beam comprising the tail of a dominant thermal core plasma, does not work. Instead, all electrons in the above-the-loop-top source seem to be accelerated, suggesting that the above-the-loop-top source is itself the electron acceleration region.

Key words: Sun: flares – Sun: particle emission – Sun: X-rays, gamma rays

Online-only material: color figures

1. INTRODUCTION

The release of magnetic energy is thought to be the source of energy for particle acceleration in solar flares. Many different acceleration mechanisms have been proposed (e.g., Miller et al. 1997), but the details of particle acceleration during solar flares remain unknown. Even the location of acceleration site is still under debate (e.g., Fletcher & Hudson 2008), although it is generally assumed to be in the corona (for a recent review, see Benz 2008). The most direct diagnostics of electron acceleration are provided by hard X-ray observations of non-thermal electron bremsstrahlung emission as the flare-accelerated electrons collide with thermal ambient protons. As bremsstrahlung emission is proportional to the ambient density, the most intense emission is observed at the chromospheric footpoints of flare loops where flare-accelerated electrons lose their energy (e.g., Hoyng et al. 1981). Coronal hard X-ray bremsstrahlung emission (see review by Krucker et al. 2008) seems to be present in most flares, but it is generally difficult to observe except in partially disk-occulted events where the intense footpoints are not visible (McKenzie 1975; Roy & Datlowe 1975; Hudson 1978; Mariska et al. 1996; Tomczak 2001, 2009; Krucker & Lin 2008). Hard X-ray spectral observations determine the number of flare-accelerated electrons (e.g., Brown 1971). The generally large numbers indicate that a large fraction of the energy released during a flare goes into electron acceleration. As the inferred flare electron spectra fall steeply as electron energy increases, most of the energy is in the difficult-to-observe low energy end of the distribution. *Reuven Ramaty High Energy Solar Spectroscopic Imager* (*RHESSI*; Lin et al. 2002) observations, with their improved spectral resolution, have extended the power-law hard X-ray spectrum to lower energies than previously known (e.g., Krucker & Lin 2002; Sui et al. 2005; Kontar et al. 2008). Especially for weak events (e.g., Krucker et al. 2002; Benz & Grigis 2002; Christe et al. 2008; Hannah et al. 2008), such as microflares, this capability gives a much clearer view of the energetics of non-thermal electrons.

The most discussed coronal hard X-ray source has been the above-the-loop-top source observed in the Masuda flare (Masuda et al. 1994), even though such events are rare (Masuda et al. 2000; Tomczak 2001, 2009; Petrosian et al. 2002; Krucker & Lin 2008). For this limb flare, the Yohkoh hard X-ray telescope (Kosugi et al. 1991) observed a coronal source in the ∼30–∼50 keV range in addition to the two hard X-ray footpoints. The coronal source was significantly (∼7 Mm) above the thermal flare loops seen in soft X-rays (hence the expression "above-the-loop-top," meaning above soft X-ray loops). No clear soft X-ray source was seen at the location of this above-the-loop-top source, indicating a rather low limit on the ambient density of the order of 10^9 cm^{-3}. The limited spectral observations favor a non-thermal interpretation (Alexander & Metcalf 1997). However, a multi-thermal explanation with temperatures up to ∼200 MK cannot completely be ruled out (Masuda et al. 1995, 2000; Tsuneta et al. 1997). Although similar time profiles are seen in the above-the-loop-top source and

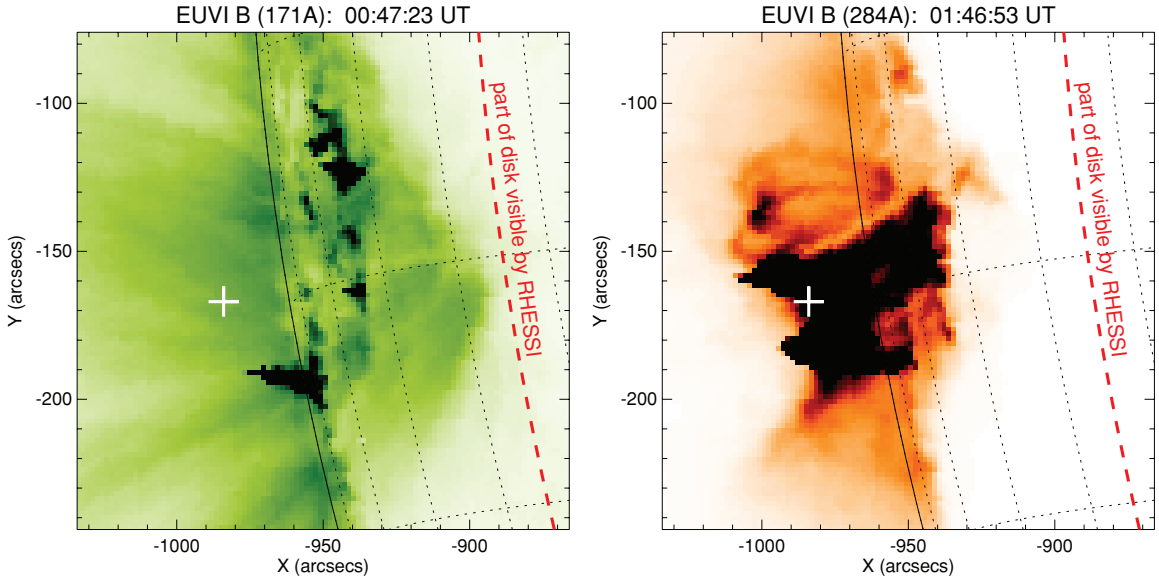

Figure 1. *STEREO* EUV imaging during the impulsive (left) and post-flare phase (right). In the impulsive phase, flare ribbons in the north–south direction are seen (note that some pixels are saturated producing artifacts in the east–west direction). The post-flare loops clearly outline the southern part of the earlier flaring ribbons, while the northern part of the ribbons is not connected by post-flare loops. The red dashed curve gives the position of the solar limb as seen from Earth perspective indicating that the flare ribbons are completely occulted from Earth perspective. The white cross marks the approximate position of the above-the-loop-top source shown in Figure 5 assuming it is located radially above the flare ribbons.

(A color version of this figure is available in the online journal.)

the footpoints, a simple thin-thick target model does not match the observations (Alexander & Metcalf 1997). Wheatland & Melrose (1995) showed that a partially thick target model could in principle work, but the low ambient density in the above-the-loop-top source does not support such a model. Introducing the combined effects of an ad hoc magnetic field convergence and pitch-angle scattering in the partially thick target model, however, can give at least partial agreement (Fletcher & Martens 1998). The scattering of electrons by plasma turbulence (e.g., Petrosian & Donaghy 1999) is another possible mechanism for enhancing the coronal hard X-ray emission, as compared to the thin target scenario. The effects of return currents could be important in these trap-and-precipitation models (e.g., Zharkova & Gordovskyy 2006; Battaglia & Benz 2007, 2008).

Electron time-of-flight measurements of the Masuda flare by Aschwanden et al. (1996) suggest that electrons at higher energies arrive systematically earlier at the footpoints than at lower energies. The derived path length is consistent with a non-thermal electron beam model with the acceleration region above the thermal loops. A thermal above-the-loop-top source could be present in a magnetic reconnection model where a reconnection jet impinges on the top of the underlying loops. This could produce a fast-mode shock that heats plasma to superhot temperatures (Masuda et al. 1994; Tsuneta et al. 1997). However, this model seems inappropriate because the above-the-loop-top source should then be seen in soft X-rays after chromospheric evaporation has filled the flare loop (e.g., Alexander & Metcalf 1997).

While other examples of above-the-loop-top sources besides the Masuda flare exist (Masuda et al. 1995; Petrosian et al. 2002; Sui et al. 2005), coronal hard X-ray sources are only very rarely seen as clearly above the thermal loops as in the Masuda flare (Tomczak 2001; Petrosian et al. 2002; Battaglia & Benz 2006; Krucker et al. 2007; Krucker & Lin 2008). In this paper, we present *RHESSI* and Nobeyama Radioheliograph (NoRH; Nakajima et al. 1994) observations of a partially disk-occulted event that shows an intense coronal hard X-ray source similar to the above-the-loop-top source in the Masuda flare. The different viewing angles provided by the *STEREO* mission (Kaiser et al. 2008) are used to study the EUV flare structures, making it possible to put the partially occulted sources seen by *RHESSI* in context with the flare loop geometry. Furthermore, the excellent spectral resolution (∼1 keV; Smith et al. 2002) of *RHESSI* provides the first detailed spectral observations of an above-the-loop-top hard X-ray source.

2. OBSERVATIONS

The flare discussed here occurred on 2007 December 31, with the *GOES* soft X-ray peak around 00:53 UT. Taking the occultation into account, the *GOES* flare classification is M2 (see Appendix A). The EUVI instrument (Howard et al. 2008) on board *STEREO B* (Kaiser et al. 2008) observed this event on-disk and revealed a two-ribbon structure (Figure 1). For *STEREO A*, the flare site was highly occulted (occultation height of ∼140 Mm) and only emission related to the associated coronal mass ejection was seen (Liu et al. 2009; de Koning et al. 2009; Antunes et al. 2009; Dai et al. 2010; Temmer et al. 2010). During the impulsive phase, the EUV flare ribbons are complex and elongated in the north–south direction (Figure 1, left), while the post-flare loops outline the southern part of the initially flaring ribbons (Figure 1, right). With the post-flare loops as a guide, the main energy release and particle acceleration must be related to the southern part of the event. The *STEREO* observations determine the flare site (defined as the location between the flare ribbons) to be ∼12° behind the solar limb from Earth perspective (Figure 2). Hence, the flare ribbons are occulted by ∼16 Mm (∼22″) from Earth perspective, and the emission detected by *RHESSI* and *GOES* therefore originates purely from the corona.

Despite the occultation, *RHESSI* observes intense hard X-ray emission up to 80 keV with a flux at 50 keV of 0.2 photons s^{-1} cm^{-2} keV^{-1} (Figure 3). The emission is most prominent during the impulsive phase, with a double-peaked

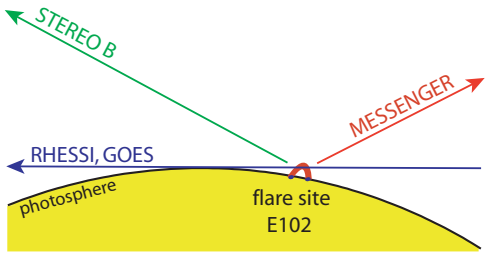

Figure 2. Flare location and view angles of the different spacecraft. *STEREO B* imaging directly reveals the flare location. From Earth perspective, the flare occurs about 12° behind the solar limb, while for *MESSENGER* the flare occurs on the solar disk.

(A color version of this figure is available in the online journal.)

main burst (00:47–00:48 UT) followed by three minor peaks (00:50:30, 00:52:30, 00:54:45 UT) with typical durations of the order of about 1 minute. Furthermore, there is also hard X-ray emission seen between 01:00 and 01:10 UT, after the soft X-ray peak time (∼00:55 UT), that will be discussed in a separate paper. Occulted flares (Krucker & Lin 2008) typically show much weaker fluxes at 50 keV, around 0.01 photons s^{-1} cm^{-2} keV^{-1} (note that for many events the 50 keV flux is an extrapolated value because the flux is below the *RHESSI* background rate). Partially occulted flares with similar flux at 50 keV to that of the 2007 December 31 flare exist, but they are rare. Compared to the above-the-loop-top source in the Masuda flare, the source in the flare described in this paper is about ∼8 times more intense at 50 keV. For comparison, typical fluxes of footpoint emission at 50 keV in an M2 class flare are around 0.8 photons s^{-1} cm^{-2} keV^{-1} (Saint-Hilaire et al. 2008, Equation (2)). Hence, the coronal hard X-ray emission from the 2007 December 31 is unusually bright and possibly could have even been detectable in the presence of hard X-ray footpoints, as was the Masuda flare.

2.1. X-ray Imaging

The thermal source structure of this event is rather complex. Several sources appear and disappear at different times in the *RHESSI* energy range below ∼10 keV (Figure 4). The interpretation of the thermal emission is further limited as neither *TRACE* (Handy et al. 1999) nor *Hinode* (Kosugi et al. 2007)

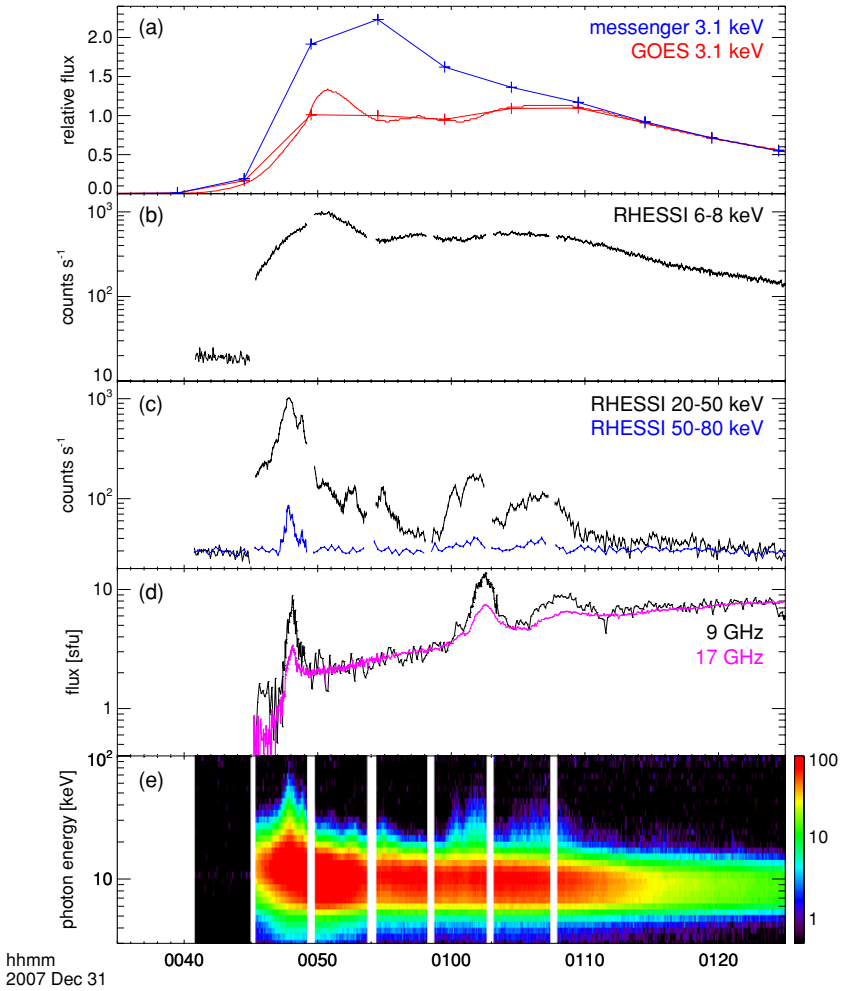

Figure 3. X-ray time profiles of the 2007 December 31 event. (a) Soft X-ray time profiles from *GOES* (red) and XRS on board the *MESSENGER* spacecraft (blue, shifted in time to account for the shorter time of flight from the Sun to the *MESSENGER* spacecraft). The *GOES* curve is shown in the original 3 s resolution, but also with the same time binning (5 minutes) as the *MESSENGER* data. The curves are normalized using the decay phase of the event (after 01:20 UT) when both instruments observed the entire emission. The lower flux observed by *GOES* during the impulsive phase is due to partial disk-occultation. (b+c) *RHESSI* hard X-ray time profiles. (d) Microwave time profiles from the NoRH at 17 GHz (magenta) and the Nobeyama Radio Polarimeter at 9 GHz (black). (e) *RHESSI* spectrogram plot with color representing count rate. *RHESSI* observations only started after 00:45 UT; for clarity, times of attenuator motions (see Lin et al. 2002) are flagged (white strips in spectrogram plot).

(A color version of this figure is available in the online journal.)

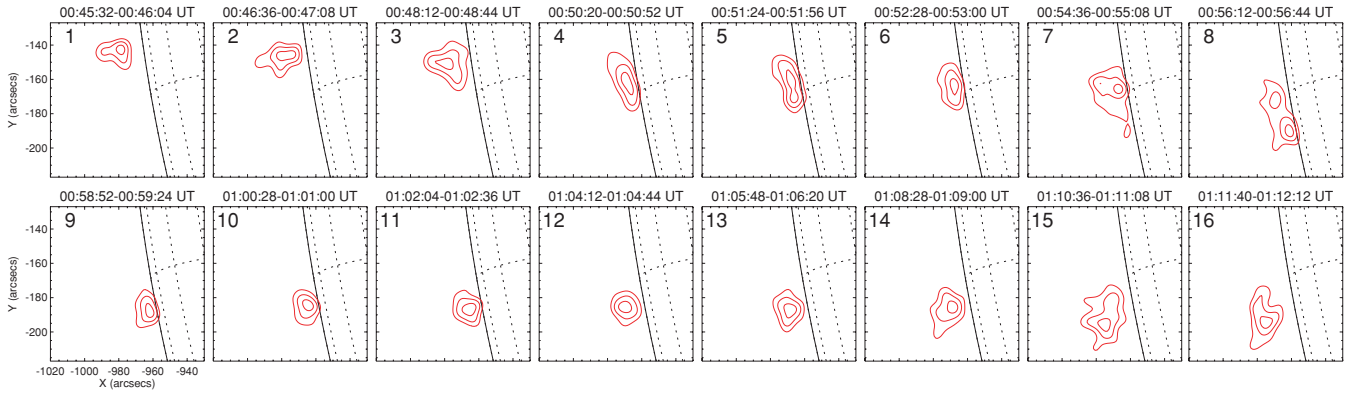

Figure 4. Thermal source structure and its temporal evolution. CLEANed images in the 6–8 keV range integrated over 32 s are shown in red (each image is scaled separately, contour levels are 50%, 70%, 90 %). Depending on the time variation of the observed sources and the occurrence of data gaps (attenuator motions), the cadence of the shown images varies between 1 and 2 minutes. The time variation is complex with several sources appearing and disappearing.

(A color version of this figure is available in the online journal.)

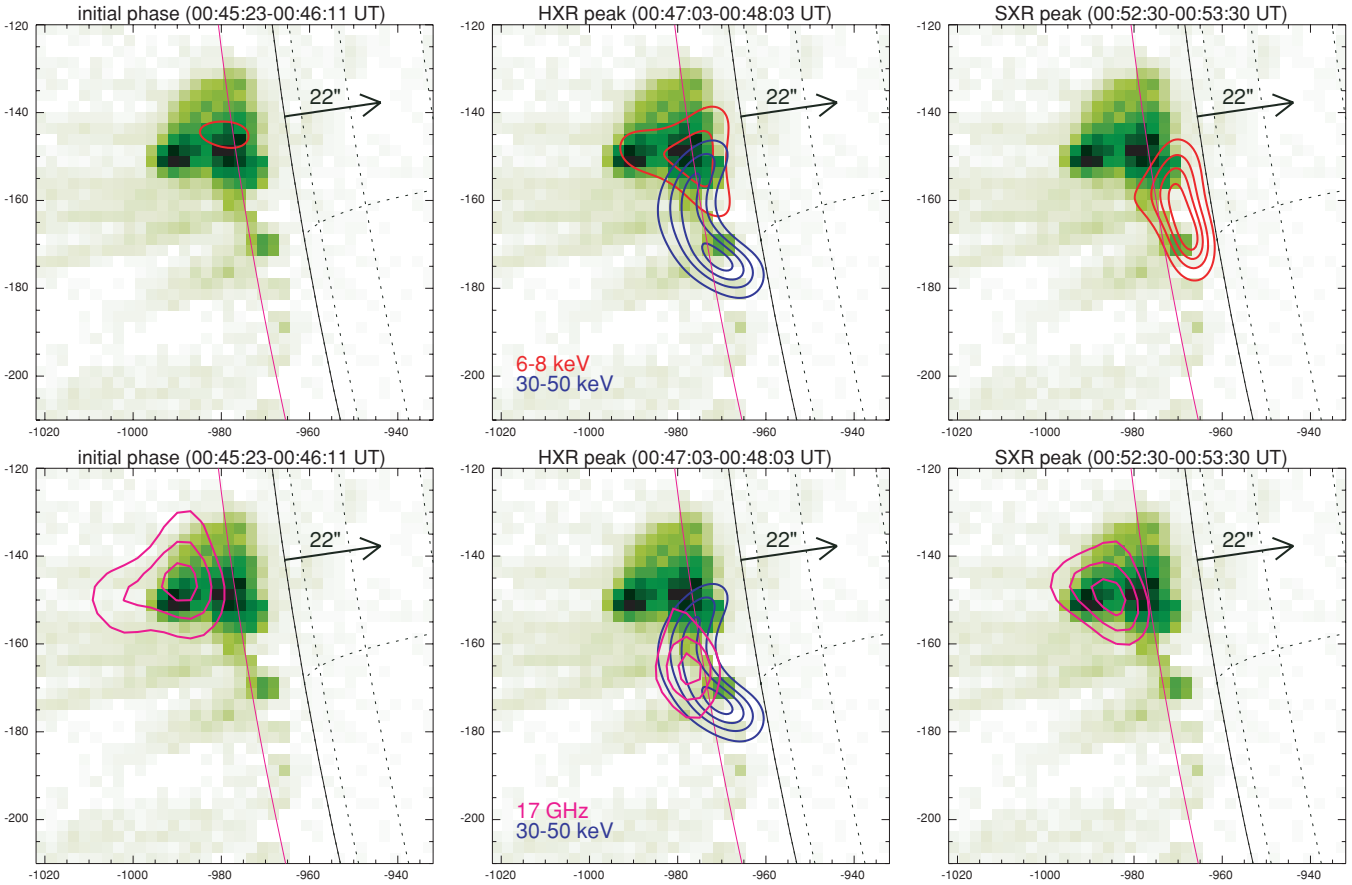

Figure 5. X-ray and microwave imaging during the initial phase (left), the hard X-ray peak (middle), and the soft X-ray peak (right). Top row: contours in the thermal (6–8 keV, red) and the non-thermal (30–50 keV, blue) range are shown on an EIT 195 Å image taken just at end of the main hard X-peak (00:48:11 UT) with the pre-flare emission taken at 00:36:10 UT subtracted. The *RHESSI* images shown are reconstructed using visibilities and a maximum entropy method (Schmahl et al. 2007). The 6–8 keV contour levels are the same for all time intervals at 20%, 40%, 60%, 80% of the maximum emission during the soft X-ray peak time, while the non-thermal emission is shown at 30%, 50%, 70%, 90 % levels. Bottom row: microwave contours (magenta) at 17 GHz are shown at the 50%, 70%, 90% levels on the same EIT image (times are 00:46:00–00:47:00 UT, 00:47:50–00:48:10 UT, 00:52:30–00:53:30 UT). For comparison, the 30–50 keV source seen during the impulsive phase is shown as well (blue). The magenta curve gives the location of the limb at 17 GHz. The black arrows indicate the occulation height. Note that the hard X-ray and microwave emission in the impulsive phase (lower center panel) occurs at higher altitude than the thermal loops seen during the soft X-ray peak time (upper right panel).

(A color version of this figure is available in the online journal.)

observations are available, and only low cadence (∼12 minutes) EUV images by EIT (Delaboudinière et al. 1995) provide some context observations. The *STEREO*/EUVI observations of the flare site itself are mostly saturated, making a detailed analysis very difficult. Even with the microwave observations from Nobeyama, only an incomplete picture of the thermal event geometry can be derived.

Before the onset of the main hard X-ray burst at 00:46:30 UT, thermal X-ray emission (∼22 MK) is seen from a coronal structure associated with EUV sources (Figure 5, left). From

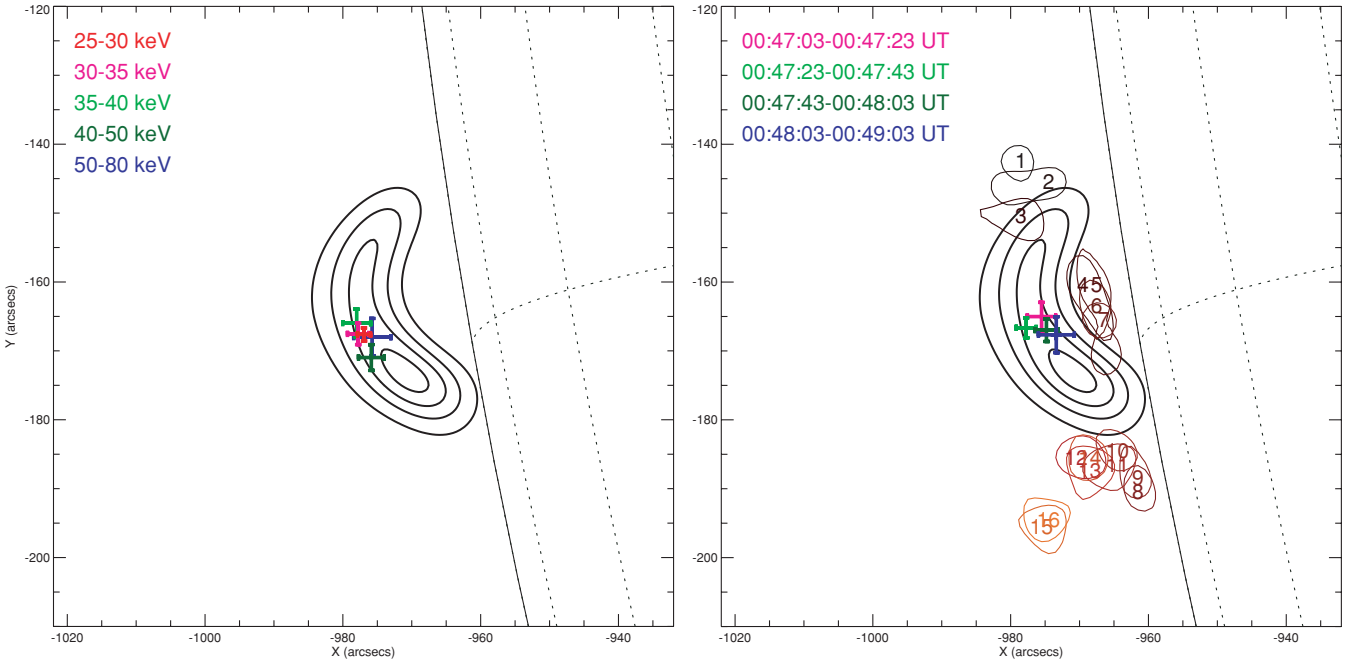

Figure 6. Left: the centroid positions at different energies during the main hard X-ray peak (00:47:03–00:48:03 UT) are shown in different colors. The positions are derived from *RHESSI* backprojection maps in the same way as described in Hurford et al. (2003). For reference the contour plot of the 30–50 keV image shown in Figure 5 is given as well. Within the uncertainties, the centroid positions are co-spatial (maximal deviation from average value is 1.6σ for the 40–50 keV centroid). Right: time evolution of the 30–50 keV centroid position during the main hard X-ray peak. No systematic source motion is found within the uncertainties. For reference, the 90% contours of the thermal images shown in Figure 4 are given. The temporal evolution is represented by color (dark red to light red) and numbers (see Figure 4).
(A color version of this figure is available in the online journal.)

the observed emission measure of this thermal X-ray source ($\sim 2 \times 10^{47}$ cm^{-3}) and the source volume ($\sim 3 \times 10^{27}$ cm^3, estimated from FWHM area to the power of 1.5), the density of the initial thermal source is of the order of $\sim 8 \times 10^9$ cm^{-3}. The >30 keV emission seen during the impulsive phase comes from a different, loop-like structure to the south of this initial thermal brightening (Figure 5, center) with source centroid clearly (~11 Mm) above the limb. Within the uncertainties, the centroid positions at different energies are all co-spatial (Figure 6, left) suggesting that the >30 keV emission comes from a single source. The >30 keV source does not show significant motion during the main hard X-ray peak (Figure 6, right). Its relation to the initial thermal source is unclear. The northern end could be connected to the early source, but projection effects could give the same appearance. In any case, the southern end of the >30 keV source is definitely from a different region without thermal X-ray emission detectable with *RHESSI* during, prior to, or after its appearance. The ambient density in the >30 keV source must therefore be rather low, but the available observations do not allow us to accurately estimate it. A rough upper limit, however, can be estimated from the hard X-ray emission of the initial source. Assuming the initial source and the thermal emission of the >30 keV source have the same temperature, the emission measure of the initial source gives a crude upper limit to the emission measure in the >30 keV source. Using the derived source volume of the >30 keV (see Table 1), an upper limit to the density of the >30 keV source becomes $n_{\rm upper} \sim 8 \times 10^9$ cm^{-3}. While the temperature prior to the hard X-ray burst could be lower, collisional losses of the hard X-ray producing electrons would rapidly heat the ambient thermal plasma (see Section 3 for details) and thermal emission from the >30 keV source during and after the hard X-ray peak should be detectable in the *RHESSI* X-ray range, if the density is high enough. Therefore, the derived upper limit should apply. Thermal emission at lower temperature prior to the hard X-ray burst could possibly also be detected by EUV and microwave observations. However, at both wavelengths, the initial source dominates the total emission (Figure 5, left) and no source that looks similar in shape and position to the >30 keV source is observed (note that the microwave emission during the hard X-ray peak is synchrotron emission; see Section 2.3 for discussion). In conclusion, the available observations suggest a low density in the >30 keV source, but no absolute value can be derived. Nevertheless, high densities ($n > n_{\rm upper}$) would produce a strong thermal X-ray source and can therefore be excluded.

A few minutes later, around the soft X-ray peak time (~00:53 UT), the thermal emission comes from a clearly different location than the initial thermal source and has an elongated shape along the limb as typically seen in partial disk-occulted events (Figure 5, right). Figure 7 shows a cartoon of the post-flare loops seen by *STEREO* in EUV (Figure 1) with the X-ray images from Figure 5 shown as contour plots projected on the plane behind the flare loops. The thermal X-ray emission seen during the soft X-ray peak roughly corresponds to the top of the flare loop with the bottom part occulted. *MESSENGER* soft X-ray observations suggest that about half of the soft X-ray flux is occulted (see Appendix A). Compared to the flare ribbons (Figure 1, right), the >30 keV source could be along the tops of the loops connecting the flare ribbons. However, projection effects make an exact interpretation difficult. In any case, the >30 keV source seen in the impulsive phase is clearly above the main flare loop seen at the soft X-ray peak around 00:53 UT (Figure 5, upper right panel). After the >30 keV source decays, it is not seen in thermal X-rays. Hence, the >30 keV source is similar to the above-the-loop-top source seen in the Masuda flare, but elongated along the flare ribbons. However, without hard X-ray observations of the footpoints and simultaneous soft X-ray observations of the main flare loop, it cannot be

Table 1
Parameters of Above-the-loop-top Sources

Parameter	Masuda Flare[a]	2007DEC31 Flare
Duration	∼2 minutes	∼2 minutes
Decay time (FWHM)	∼30 s	∼40 s
Energy range	∼25–50 keV	∼16–80 keV
Flux at 50 keV (ph s^{-1} cm^{-2} keV^{-1})	∼0.02	∼0.2
Height above photosphere	∼20 Mm	∼27 Mm
Height above flare loop	∼7 Mm	∼6 Mm
Length	∼5 Mm	∼29 Mm
Width	∼5 Mm	∼6 Mm
Volume[b]	$\sim 1 \times 10^{26}$ cm^3	$\sim 8 \times 10^{26}$ cm^3
Pre-flare ambient density[c]	low	low
γ at hard X-ray peak time	4-5.5	∼4.2
Electron spectral index, δ_{thin}	3-4.5	∼3.7
Non-thermal electron density[d]	$\sim 2 \times 10^9$ cm^{-3}	$\sim 2 \times 10^9$ cm^{-3}
Energy in non-thermal electron	$>1 \times 10^{28}$ erg	$>1 \times 10^{29}$ erg
Superhot temperature[e]	∼100 MK	∼200 MK
Superhot emission measure[e]	$\sim 1 \times 10^{44}$ cm^{-3}	$\sim 9 \times 10^{44}$ cm^{-3}
Superhot density[e]	$\sim 1 \times 10^9$ cm^{-3}	$\sim 1 \times 10^9$ cm^{-3}
Superhot thermal energy content[e]	$\sim 4 \times 10^{27}$ erg	$\sim 7 \times 10^{28}$ erg
Flux at 17 GHz		∼1.7 sfu
α at peak time		∼1.8
Electron spectral index, δ_μ		∼3.4
Typical energy of 17 GHz producing electrons		∼1.2 MeV
Estimated magnetic field strength		∼30–50 G
Pre-flare plasma beta[f]		∼0.01
Plasma beta in hard X-ray source		∼1

Notes.
[a] Parameters taken from Masuda et al. (2000). The differences compared to the original publication (Masuda et al. 1994) reflect the improved calibration used in Masuda et al. (2000).
[b] Volume = length × width^2.
[c] For the case that all electrons are accelerated, the pre-flare density is equal to the non-thermal density given below.
[d] Derived assuming all electrons are accelerated.
[e] Thermal interpretation is inconsistent with microwave observations.
[f] Assumes a pre-flare temperature of 2 MK.

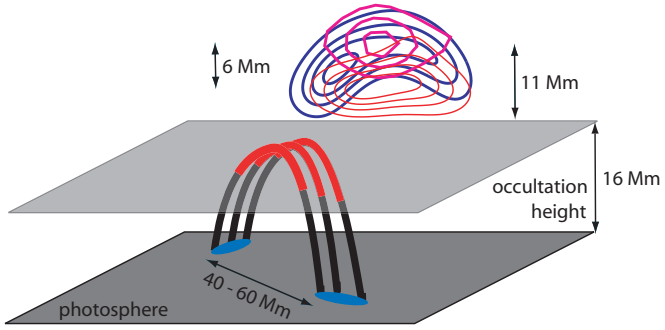

Figure 7. Cartoon of the impulsive phase of the 2007 December 31 flare. The dark gray plane is the photosphere, while the parallel plane in lighter gray gives the occultation height of the *RHESSI* observations. The flare loops are shown in black with the top part visible by *RHESSI* colored red. The contours of the hard X-ray and microwave images from Figure 5 are shown projected on the plane behind the flare loops. Source sizes and altitudes are roughly to scale.
(A color version of this figure is available in the online journal.)

unambiguously established that the >30 keV source is indeed the same type of coronal source as the above-the-loop-top source in the Masuda flare.

2.2. X-ray Spectra

During the impulsive phase (00:47:42–00:47:50 UT), the hard X-ray photon spectrum is well represented by a single thermal and a broken power-law fit ($\chi^2 \sim 1.1$ for the spectral fit shown in Figure 8, left). The power-law fits show a clear soft-hard-soft behavior (Figure 9, right), similar to the typical spectral behavior of most footpoint spectra (e.g., Grigis & Benz 2004). The hardest/flattest spectrum at the peak of the emission has a photon spectral index $\gamma \sim 4.2 \pm 0.1$. Compared to statistical results for flares with similar occultation heights (Krucker & Lin 2008), this event is among the ones with the hardest/flattest spectra. Below 16 keV, thermal emission originating from the initial bright source dominates the spectra, making it impossible to get accurate flux estimates for the low-energy component of the >30 keV source. At the location of the >30 keV source, the 10–12 keV image does not show an identifiable source above the noise level of ∼20%. Extrapolating the power-law fit to energies below 16 keV (dotted blue line in Figure 8) predicts that the >30 keV source should be 45% of the total emission in the 10–12 keV range. Hence, the non-detection of the >30 keV source in the 10–12 keV image suggests that there is a turnover at energies not too far below the fitted value of ∼16 keV. A further indicator of the existence of a low-energy cut-off is that the 6–8 keV light curve shown in Figure 3 has a completely different temporal evolution than the 20–50 keV light curve. If the power-law fit were to extend down to ∼6 keV as shown in Figure 8 (dotted blue curve), the 6–8 keV light curve would have a component at the ∼10% level with a time profile similar to the 20–40 keV emission. Since this is not the case, there is likely to be a turnover in the power-law spectrum.

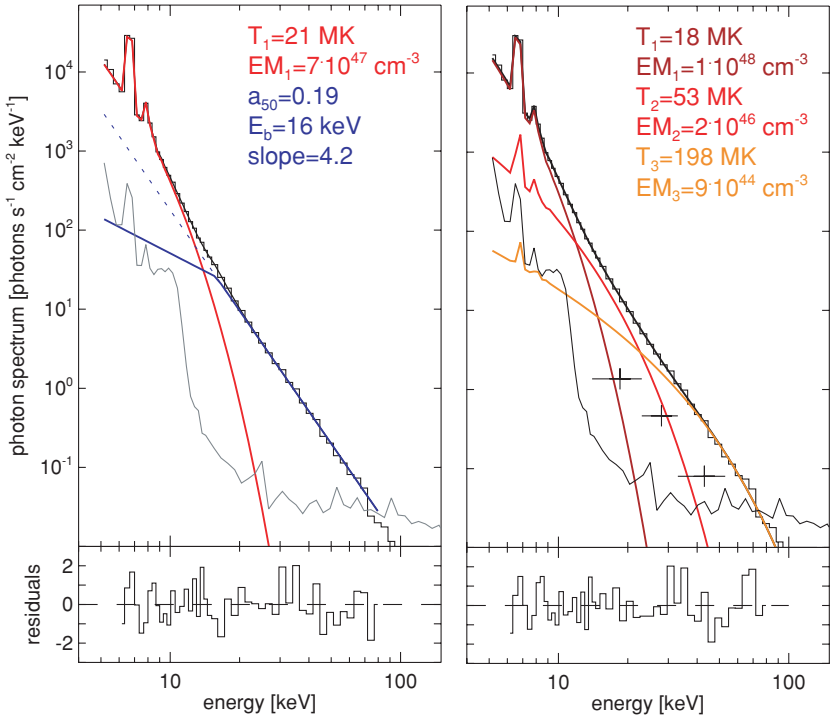

Figure 8. Spectral fitting during the hard X-ray peak (00:47:42–00:47:50 UT). The data are shown as histograms and the sum of all fitted components is given as the solid black line. The residuals of the fit in units of the standard deviation derived from photon statistics are shown on the bottom panel of each plot. Left: thermal (red) and broken power-law fit with a fixed slope of 1.5 below the break (blue). The dotted blue curve is the low-energy extension of the power-law fit above the break. Right: multi-thermal fit given by three different shades of red (see Appendix B). The three black points with error bars give the spectrum of the Masuda flare.

(A color version of this figure is available in the online journal.)

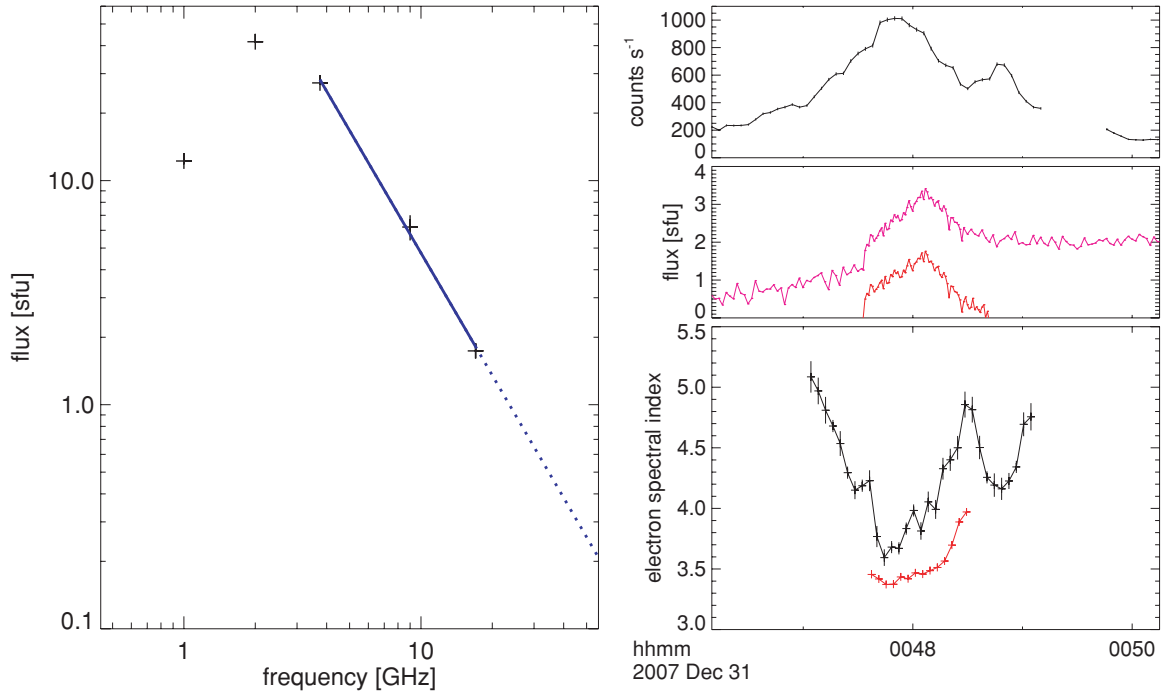

Figure 9. Left: microwave spectrum during the impulsive phase (00:48:00–00:48:04 UT) with the thermal emission seen before and after subtracted (linear interpolation). The blue curve gives a power-law fit to the fluxes above 3.75 GHz with a slope of ∼1.8. Right: the bottom panel shows the temporal evolution of the electron spectral indices derived from hard X-ray (black) and microwave (red) observations. The two panels above give the hard X-ray (20–50 keV, black) and microwave (17 GHz, magenta) time profiles for comparison (same as in Figure 3). The red curve is the 17 GHz time profile after subtraction of the thermal emission. The subtraction of the thermal emission introduces significant uncertainties (∼0.3) in the spectral indices derived from the radio observations at the end of the burst (after 00:48:24 UT), while the derived value at peak time only slightly (∼0.1) depends on the subtraction of the thermal emission.

(A color version of this figure is available in the online journal.)

Using the power-law fit to the photon spectrum at peak time ($\gamma = 4.2$ and flux at 50 keV of 0.2 ph s^{-1} cm^{-2} keV^{-1}, see Table 1) and the upper limit of $E_0 = 16$ keV as a cutoff energy, the derived instantaneous number of electrons at peak time (e.g., Lin 1974, Equation (2.4)) becomes $N_{\rm inst} = 4 \times 10^{36} n_9^{-1}$ $[E_0/16\ {\rm keV}]^{-2.7}$, where n_9 is the ambient density in units of 10^9 cm^{-3}. During the main hard X-ray peak (00:47–00:48 UT), the instantaneous number shows relatively little time variation with values between (3–4)$\times 10^{36}$ n_9^{-1}. From the observed size of the >30 keV source (for details about source size determinations from *RHESSI* observations, see Dennis & Pernak 2009), a volume of $\sim 8 \times 10^{26}$ cm^3 is derived assuming the thickness of the source is equal to the width (see Table 1), and the instantaneous non-thermal electron density becomes $n_e = 5 \times 10^9 n_9^{-1}$ $[E_0/16\ {\rm keV}]^{-2.7}$. The ratio of the non-thermal to thermal density in the >30 keV source then is $R \equiv n_e/n > 0.1$ $[n_{\rm upper}/n]^2 [E_0/16\ {\rm keV}]^{-2.7}$, where $n_{\rm upper} \sim 8 \times 10^9$ cm^{-3} is the upper limit of the thermal density derived in Section 2.1. Although a filling factor for the non-thermal source would increase n_e, a filling factor also affects our estimates of the upper limit of the density, and the two effects cancel. A filling factor should therefore not change our estimates of R. Hence, we conclude that the non-thermal electrons are not simply a tail on the thermal distribution, but would even outnumber the thermal electrons for plausible densities below $\sim 2 \times 10^9$ cm^{-3}.

2.3. Microwave Observations

The bottom row of Figure 5 shows microwave images at 17 GHz for the three time intervals discussed in Section 2.1. At 17 GHz the radius of the effective solar limb is fitted to be 1.0125 times the photospheric radius (Hanaoka et al. 1994; Gary 1996), i.e., a height of 9 Mm above the optical limb, and the occultation height for the 17 GHz observations is therefore ~25 Mm. Before the hard X-peak, the 17 GHz emission shows the same source as seen in thermal X-ray and EUV (Figure 5, bottom left). During the hard X-peak, the 17 GHz emission is co-spatial with the >30 keV source (Figure 5, bottom center), but the larger occultation height only allows us to observe the top part of the source. The main flare loop seen during the soft X-ray peak time is occulted in the 17 GHz observations and emission from the initial source continues through the soft X-ray peak time (Figure 5, bottom right). While the radio emission from the location of the initial source has the same flux density at 9 GHz and 17 GHz (Figure 3), consistent with thermal bremsstrahlung emission (e.g., Dulk 1985), the microwave spectrum during the hard X-ray peak decreases with frequency as expected for gyrosynchroton emission (Figure 9, left). This clearly favors a non-thermal interpretation for the above-the-loop-top source. The peak frequency of ~2.5 GHz is low compared to on-disk flares, which typically show peak frequencies above 10 GHz, consistent with the lower magnetic field strength expected in a coronal source (e.g., Hudson 1978; for estimation of the magnetic field strength, see Section 3). A power-law fit to the fluxes at 3.75, 9, and 17 GHz gives a slope of $\alpha \sim 1.8$ at the peak of the event. Using the gyrosynchrotron approximation by Dulk & Marsh (1982, Equation (13)), $\delta \sim 1.1\alpha + 1.4$, the gyrosynchroton-producing electrons have a power-law index of $\delta \sim 3.4$.

3. DISCUSSION

Although the flare geometry of the present event is difficult to reconstruct, the impulsive phase clearly shows a coronal hard X-ray source up to ~80 keV located ~6 Mm above the main thermal flare loops. It thus resembles the Masuda flare (Table 1). The elongated shape could be explained by emission along the flare arcade and not only from a single location as in the Masuda flare (note that the Masuda source itself could have been a loop-top arcade in projection). Below 16 keV, thermal emission from a different location that brightens earlier masks any possible X-ray emission from ambient thermal plasma in the above-the-loop-top source. From the hard X-ray observations (Section 2.1), we derive an upper limit for the ambient density in the above-the-loop-top source of 8×10^9 cm^{-3}. For all plausible densities, the ratio R of numbers of the hard X-ray producing electrons to the ambient thermal electrons is roughly of the order of unity. Hence, the scenario of an electron beam as an insignificant tail of a dominant thermal core distribution is not an appropriate description. Since most of the energy is in non-thermal electrons, the collisional energy deposition even in the thin target approximation would rapidly heat the ambient electrons. Using the energy deposition rate in the thin target model (e.g., McKenzie et al. 1973; Lin 1974), the rate of energy increase for an ambient electron is $\epsilon_{\rm thin} = 4.5\, n_9^{-1}$ keV s^{-1}. Even for upper limit $n_9 = 8$, this corresponds to a heating rate $dT/dt \sim 5$ MK s^{-1}, and the heating persists for tens of seconds. In the thick target scenario (this requires that the accelerated electrons be confined in the hard X-ray source), the heating rate is even larger (see Appendix C). Hence, the ambient electrons rapidly acquire energies similar to those of the non-thermal electrons. Such a rapid energization of the electrons could be avoided if there is heat transport out of the hard X-ray source, but the plasma physics of such a process is not understood. Therefore, the electron distribution in the hard X-ray source is more likely purely non-thermal, without any thermal electron distribution.

The same conclusion can be drawn for the above-the-loop-top source in the Masuda flare. For the Masuda flare, the above-the-loop-top source has a spectral shape similar to that of the event presented here (Figure 8) but is about 8 times weaker, and the source volume is ~8 times smaller. Hence, for the same cutoff energy of 16 keV, R is of the same order of magnitude for the event presented here.

In the scenario where all electrons are accelerated, the pre-event density n_0 is the same as the density of accelerated electrons n_e. Hence, using $n_0 = n_e$, the derived instantaneous number of radiating electrons (Section 2.2), and the estimated source volume (Table 1) the density becomes $n_e = 2 \times 10^9 [E_0/16\ {\rm keV}]^{-1.35} {\rm cm}^{-3}$, where E_0 is the cutoff energy. This density is below the derived upper limit of 8×10^9 cm^{-3}, suggesting that if the same source were to radiate the same temperature as the initial thermal source before or after the non-thermal hard X-ray burst, its emission measure would be ~16 times smaller than the initial thermal source. Thermal X-ray emission from the >30 keV source would therefore be lost in the limited dynamic range of *RHESSI* images (the dynamic range of the presented thermal images in Figure 5 is ~5, i.e., contours below 20% show noise). The instantaneous number of non-thermal electrons above 16 keV (see Section 2.2) then becomes $N_{\rm inst} = 2 \times 10^{36} [E_0/16\ {\rm keV}]^{-2.7}$ with a total energy content of $0.8 \times 10^{29} [E_0/16\ {\rm keV}]^{-0.35}$ erg. These values are lower limits of the total electron number and energy. Depending on how many non-thermal electrons escape the above-the-loop-top source during the hard X-ray peak duration, the total number of electrons $N_{\rm tot}$ could be significantly larger than $N_{\rm inst}$. The fastest escape time is the source transit time of ~0.4 s (here we used an electron energy of 16 keV and the observed length of

>30 keV source of 29 Mm). Hence, during the 120 s duration of the main hard X-ray peak, the total volume would have to be replaced about 300 times giving $N_{\rm tot} \sim 300 N_{\rm inst}$. However, such a large escape rate would require very fast replenishment of electrons. In the following, we try to estimate escape rates from the observed hard X-ray time profiles (Figure 9). As the observed time profiles represent a convolution of acceleration, energy losses, and the interplay between confinement and escape (see also discussion in Section 3.1), a characteristic escape time can only be estimated by making further simplifications. We assume that the escape of electrons is the dominant energy loss mechanism. Further assuming a constant escape rate during the rise and decay of the hard X-ray peak and that acceleration is turned off during the decay, the roughly equal duration of rise and decay phase of the hard X-ray time profile suggests that the same number of electrons are escaping during the rise as the decay and $N_{\rm tot} \sim 2N_{\rm inst}$. Using the fastest observed decay time (around 00:48:55 UT with an exponential decay time of 17 s) as an approximation of the escape time gives $N_{\rm tot} \sim 7N_{\rm inst}$. Therefore, the total energy in non-thermal electrons could be significantly larger than the instantaneous value of 0.8×10^{29} erg, and it could be possible that there is enough energy to account for the thermal energy observed in the main flare loop ($>3 \times 10^{29}$ erg; see Appendix B), but the available data are not conclusive.

The microwave observations during the hard X-ray peak time show that the electron distribution in the above-the-loop-top source is non-thermal with a power-law distribution with index $\delta_\mu \sim 3.4$. The hard X-ray photon spectrum taken at the same time can also be well represented by a power law with index $\gamma \sim 4.2 \pm 0.1$. Even in the absence of ambient thermal electrons, the thin-target approximation is still valid, and the power-law index of the non-thermal electrons becomes $\delta_{\rm thin} \sim \gamma - 0.5 = 3.7 \pm 0.1$. The time evolution of the electron spectral index derived from hard X-ray and microwave observations is shown in Figure 9 (right). While both methods show similar time variations, the microwave observations give slightly harder/flatter spectra. The simplifying assumptions made, in particular in the derivation of the power-law index from the microwave observations (see Dulk & Marsh 1982), could introduce systematic uncertainties of the same order as the observed differences. In any case, a similar power-law index must extend over a large range of energies, from ~16 keV up to the MeV range.

In the following, the magnetic field strength in the microwave source is estimated using the approximation by Dulk (1985). In addition to the parameters derived above (δ and n_e), the angle between the magnetic field and the line of sight needs to be known. The post-flare loops have about a ~45° angle to the line of sight (Figures 1 and 5). However, the magnetic field direction in the above-the-loop-top region could be different. The current sheet in magnetic reconnection models suggest field lines close to the radial direction, giving $\theta \sim 90°$. Low values of θ (i.e., magnetic field lines along the line of sight), however, are difficult to imagine for the December 31 flare. In the following a value of $\theta = \theta_{45} = 45°$ is used. From the observed roll-over frequency (~2.5 GHz) of the microwave spectrum, the magnetic field strength in the above-the-loop-top source can be estimated to be $\sim 30 \sin(\theta_{45})^{-0.65}$ G (Dulk 1985, Equation (39), using a length along the line of sight of 6 Mm, $\delta = 3.4$, and the non-thermal electron density of 2×10^9 cm^{-3}). A further estimate of the magnetic field can be derived using the observed microwave flux giving $B \sim 40 \sin(\theta_{45})^{-0.63}$ G (Dulk 1985, Equation (35), using a solid angle of 1.6×10^{-9} sr and the same values as above). Unfortunately, the dependence of θ is very similar for both expressions of B, so that it is not possible to determine a consistent value of θ within the uncertainties. However, the derived values of the magnetic field strength are similar for both cases, and for plausible values of θ ($\sim 30° < \theta < 90°$) the magnetic field strength is between ~30 and ~50 G. The characteristic energy of the electrons producing the 17 GHz emission then becomes ~1.2 MeV (Dulk 1985, Equation (37)). Combined with the estimated ambient density of 2×10^9cm^{-3}, the derived magnetic field strength gives a pre-event plasma beta between ~0.005 and ~0.02 for a pre-flare plasma temperature of 2 MK. In the >30 keV source, the energy density of the accelerated non-thermal electrons replaces the energy density of the thermal population and the effective plasma beta becomes ~1. Hence, the energy density in electrons has increased by two decades and become comparable to the energy density in the magnetic field.

3.1. Discussion of Models

The following five main points must be considered by a model of an above-the-loop-top hard X-ray source.

1. The acceleration site is in a coronal low-β plasma located above (~6 Mm) the main thermal flare loops seen in soft X-rays.
2. The acceleration region does not emit significantly at EUV and soft X-ray wavelengths (i.e., the density of the acceleration region is low and does not increase significantly during the impulsive phase of flare).
3. All of the electrons are accelerated into a power-law distribution extending up to the MeV range.
4. The energy density of non-thermal electrons is of the same order of magnitude as the magnetic energy density (i.e., $\beta \sim 1$).
5. Accelerated electrons need to be released on time scales of the hard X-ray decay (~40 s). However, some confinement might be needed as well, as otherwise the number of accelerated electrons needed to produce the observed hard X-ray emission becomes excessively large.

Shrinking of thermal flare loops during the impulsive phase as reported for several events (Sui & Holman 2003; Krucker et al. 2003; Sui et al. 2004; Liu et al. 2004; Veronig et al. 2006) could in principle be responsible for observing the main thermal loop at lower altitude. Loop shrinkage is not fully understood, although it seems to follow naturally from the requirement for the release of magnetic energy (Hudson 2000). It could be due to (1) relaxation of newly reconnected field lines (collapsing magnetic trap model, e.g., Somov & Kosugi 1997), (2) the onset of fast Petscheck-type reconnection (Sui et al. 2004), or (3) relaxation of the shear in magnetic field lines (Ji et al. 2007). Loop shrinkage is generally seen as a continuous motion of thermal emission from higher to lower altitude for a few minutes followed by an increase in altitude that exceeds the initial starting point within a few minutes. This is different from what is reported here, where a non-thermal source is seen first without detectable thermal emission, followed by a thermal source seen at lower altitude. Hence, two distinct sources are seen. Nevertheless, loop shrinking and the existence of above-the-loop-top sources could be linked and deserve further investigations, but the available observations for the event presented here does not allow us to draw further conclusions.

The points listed above excludes all simple thermal models, in particular the reconnection scenario where the reconnection jet interacts with the previously created flare loops producing a superhot plasma (Masuda et al. 1994; Tsuneta et al. 1997) and dissipative thermal models (Brown et al. 1979; Smith & Lilliequist 1979; Vlahos & Papadopoulos 1979; Emslie & Vlahos 1980; MacKinnon 1985). However, a similar scenario with an entirely non-thermal coronal source instead of thermal one could possibly be of interest. The large number of non-thermal electrons ($R > 0.1$) also excludes non-thermal models where electron beams produce the above-the-loop-top source. Trap-and-precipitation models only work if the trap region is the acceleration region itself (e.g., Xu et al. 2008).

More promising are mechanisms involving acceleration by turbulence created by the reconnection process (e.g., Benz 1977; Ramaty 1979; Hamilton & Petrosian 1992; Miller et al. 1996; Petrosian & Liu 2004; Grigis & Benz 2008). In this scenario, the acceleration region is given by the location of high turbulence and could possibly be significantly above the flare loops (for a cartoon, see Figure 1 in Liu et al. 2008). A similar geometry could exist in the acceleration model where electrons gain energy through Fermi acceleration in contracting magnetic islands created during the reconnection process (e.g., Drake et al. 2006). These islands could be volume-filling in a region around a large-scale X-line, so that essentially all electrons entering the multi-island region would be accelerated. Electrons can be confined in these islands, jump from island to island, or escape the region filled with magnetic islands and precipitate to the footpoints. The resulting electron distribution is a power law. This model works best for low values of pre-event plasma beta ($\beta \ll 1$). Island contraction and therefore acceleration stops when electron energy density becomes similar to the magnetic energy density ($\beta \sim 1$), similar to what we find in this event.

We can roughly estimate electron number and energy in a reconnection scenario, using the observed geometry. A lower limit for the area of a hypothetical inflow of thermal electrons into the multi-island region (we note that the EUV images around the time of the impulsive phase show no evidence for inflows) can be approximated from the observed length l and width w of the hard X-ray source (for a cartoon, see Figure 4 in Drake et al. 2006), and the rate of electrons flowing into the multi-island region becomes $2n_e v_{\rm in} lw \sim 6 \times 10^{34}$ electrons per second, where $v_{\rm in} \sim 0.1 c_a$ and c_a is the Alfvén speed (see Drake et al. 2006). Hence, during the duration of the impulsive phase ($\sim$120 s), a total of $\sim 8 \times 10^{36}$ electrons could be provided to the above-the-loop-top source (return currents could provide further replenishment of escaping electrons). This corresponds to more than 5 times the number of electrons in the above-the-loop-top source before the flare (Table 1). Assuming again an inflow velocity of $\sim 0.1 c_a$, the total magnetic energy flowing into the above-the-loop-top source can be estimated to $\sim 5 \times 10^{29}$ $[B/40\ {\rm G}]^2$ erg (e.g., Isobe et al. 2002). Since the inflow region could be larger than the hard X-ray source size, the reconnection inflow could possibly provide enough electrons and magnetic energy. The derived values of magnetic energy are only marginally comparable to flare energy and would therefore require a very efficient release of magnetic energy.

4. SUMMARY

The partially disk-occulted flare of 2007 December 31 presented in this paper provides detailed hard X-ray and microwave observations of a coronal hard X-ray source similar to the above-the-loop-top source in the Masuda flare. As the number of hard X-ray producing electrons is found to be very large, the standard electron beam scenario does not work. The main problems are that the number of accelerated electrons is comparable to the total number of electrons in the pre-flare source and that collisional heating would increase the ambient plasma temperature to superhot temperatures within seconds. The same conclusion holds for earlier observations of above-the-loop-top sources, but it was not recognized, presumably because the heating in the thin-target scenario was generally assumed to be negligible. While the collisional losses in the thin-target scenario are negligible compared to the total energy of the electron beam, they significantly and rapidly increase the temperature of the ambient plasma, especially for low ambient densities.

The above-the-loop-top source rather is therefore produced by a mechanism that accelerates all electrons and produces an entirely non-thermal electron distribution. This suggests that the above-the-loop-top source is the acceleration region itself. Estimates of the pre-flare or post-flare density of the above-the-loop-top source could further corroborate this scenario. The available observations for the December 31 flare unfortunately only allowed us to derive an upper limit. Future observations, in particular with *Hinode* and Solar Dynamics Observatory, should be able to provide density measurements at different temperatures via spectroscopy and multi-wavelength EUV imaging.

In a purely non-thermal electron distribution, collisional losses to electrons are much reduced, making it an efficient hard X-ray source. Once a significant fraction of the electrons is accelerated, collisional losses of an accelerated electron are reduced due to a smaller number of ambient electrons. This simple picture suggests that once a significant fraction of the electrons is accelerated, it might not take that much more to accelerate all of the electrons. We speculate that above-the-loop top sources are only visible once all electrons are accelerated. For events with less efficient acceleration or for events with a large escape rate of accelerated electrons from the acceleration site, the acceleration site is expected to be relatively faint in hard X-ray emission, below present-day detection limits.

We thank the anonymous referee, and Brian Dennis, Gordon Holman, and Eduard Kontar for critical comments. The work has been supported by NASA contract NAS 5-98033 and NNG05-GI-91G for *RHESSI* and partially by the WCU grant (No. R31-10016) funded by the Korean Ministry of Education, Science, and Technology.

APPENDIX A

MESSENGER SOFT X-RAY OBSERVATIONS

A rough estimate of the fraction of occulted soft X-ray emission can be derived by comparing the partially occulted soft X-ray observations from *GOES* with soft X-ray measurements from the X-ray spectrometer (XRS; Schlemm et al. 2007) on board *MESSENGER*, in a position to observe the entire emission (Figure 2). The temporal evolution of the decay phase agrees well between these instruments (Figure 3, top), suggesting the total emission is seen by both after $\sim$01:10 UT. *RHESSI* imaging shows that the thermal source at $\sim$6 keV is indeed entirely above the limb after $\sim$01:10 UT (Figure 4), confirming that *RHESSI* and therefore also *GOES* observed most of the emitted flux. During the impulsive phase, however, the *GOES* flux is lower by about a factor of 2.2 relative to *MESSENGER* (after adjustment for the different distances to the Sun), suggesting that the flux seen by *GOES* and *RHESSI* is only about $\sim$45% of the total flux.

Hence, the reported *GOES* class of C8 for the partially occulted flare corresponds to that of an occulted M2 event. Furthermore, the latter increases in the *GOES* time profiles around 00:58 UT and 01:06 UT are likely to be due to flare loops seen further and further above the limb, and not due to increased flare emission.

APPENDIX B

X-RAY SPECTRA: MULTI-THERMAL FITS

Although microwave observations strongly suggest a non-thermal electron distribution, hard X-ray spectral fits using (in addition to the usual thermal fit that dominates below ∼10 keV) thermal components with higher temperatures (so-called superhot components) are discussed here for completeness. Adding just one more superhot component, as done for the Masuda flare (Masuda et al. 1995; Tsuneta et al. 1997; Masuda et al. 2000) cannot represent the data. Adding a third thermal component represents the data as well as the power-law fit discussed above with $\chi^2 \sim 1.1$ (Figure 8, right), although one more fit parameter is used. One of these superhot components covers the highest energies and the other one fills in the gap in between. While the fits are satisfactory, the lower-temperature superhot component had not previously been required as a part of a theoretical model. Most (∼88% of the total flux) of the >30 keV source shown in Figure 5 is represented by the hottest temperature component with ∼200 MK and EM $= 9 \times 10^{44}$ cm^{-3}. The time evolution of the superhot component during the rise phase of the hard X-ray emission shows an increase in temperature (from ∼100 to ∼200 MK) and slight decrease of emission measure (20×10^{44} cm^{-3} to 9×10^{44} cm^{-3}), while the decay phase shows the reverse effect. This clearly excludes an adiabatic compression scenario where emission measure and temperature are expected to increase and decrease simultaneously (Maetzler et al. 1978, Equation (9)).

Using the estimated source volume (∼8×10^{26} cm^3), the density of the superhot component becomes ∼1×10^9 cm^{-3} for a filling factor of unity, and the thermal energy content of super hot plasma is 7×10^{28} erg. The lower-temperature superhot component with a ∼4 times lower temperature, but a ∼20 times higher emission measure has roughly the same thermal energy. For comparison, the thermal energy in the main flare loop at the soft X-ray peak ($T \sim 19$ MK, EM $\sim 2 \times 10^{48}$ cm^{-3}, $V \sim 5 \times 10^{26}$ cm^3, $n \sim 6 \times 10^{10}$ cm^{-3}) is 3×10^{29} erg plus the energy in the occulted part (roughly a factor of 2, see Appendix A). Hence, the energy in the superhot component is about an order of magnitude less than the thermal energy content in the main flare loop. However, energy loss mechanisms are not considered in this comparison. If the superhot component loses energy during the impulsive phase, it would need to be further heated to account for the losses and the total energy could therefore be significantly larger. The same holds for the calculation of the thermal energy content of the main flare loop, but a less severe requirement because of the temperature dependence of the probable cooling mechanisms.

APPENDIX C

THICK TARGET APPROXIMATION

Thick target coronal hard X-ray sources are reported for some flares (Veronig & Brown 2004), but are rather rare. These events have steep hard X-ray spectra with power-law indices between 6 and 7, and high ambient densities of 10^{11} cm^{-3} (e.g., Bone et al. 2007). The event discussed here has many different parameters (Table 1). Therefore, the thick target approximation can only be applied to the December 31 flare if the accelerated electrons are confined in the corona. Then the time-integrated spectrum over the main hard X-ray peak could be treated as thick target emission. For a 16 keV cut-off energy, the energy deposition rate becomes 3×10^{28} erg s^{-1} (2×10^{30} erg for the total event). The resulting heating rate of 9 n_9^{-1} keV s^{-1} is again very fast and the same argument as in the thin target approximation suggests that all electrons are accelerated. As collisional losses to electrons are drastically decreased if all electrons are accelerated, the thick target approximation (which assumes collisional losses to electrons to be the dominant loss mechanism) breaks down.

REFERENCES

Alexander, D., & Metcalf, T. R. 1997, ApJ, 489, 442
Antunes, A., Thernisien, A., & Yahil, A. 2009, Sol. Phys., 259, 199
Aschwanden, M. J., Hudson, H., Kosugi, T., & Schwartz, R. A. 1996, ApJ, 464, 985
Battaglia, M., & Benz, A. O. 2006, A&A, 456, 751
Battaglia, M., & Benz, A. O. 2007, A&A, 466, 713
Battaglia, M., & Benz, A. O. 2008, A&A, 487, 337
Benz, A. O. 1977, ApJ, 211, 270
Benz, A. O. 2008, Living Rev. Solar Phys., 5, 1
Benz, A. O., & Grigis, P. C. 2002, Sol. Phys., 210, 431
Bone, L., Brown, J. C., Fletcher, L., Veronig, A., & White, S. 2007, A&A, 466, 339
Brown, J. C. 1971, Sol. Phys., 18, 489
Brown, J. C., Spicer, D. S., & Melrose, D. B. 1979, ApJ, 228, 592
Christe, S., Hannah, I. G., Krucker, S., McTiernan, J., & Lin, R. P. 2008, ApJ, 677, 1385
Dai, Y., Auchère, F., Vial, J.-C., Tang, Y. H., & Zong, W. G. 2010, ApJ, 708, 913
de Koning, C. A., Pizzo, V. J., & Biesecker, D. A. 2009, Sol. Phys., 256, 167
Delaboudinière, J.-P., et al. 1995, Sol. Phys., 162, 291
Dennis, B. R., & Pernak, R. L. 2009, ApJ, 698, 2131
Dulk, G. A. 1985, ARA&A, 23, 169
Dulk, G. A., & Marsh, K. A. 1982, ApJ, 259, 350
Drake, J. F., Swisdak, M., Che, H., & Shay, M. A. 2006, Nature, 443, 553
Emslie, A. G., & Vlahos, L. 1980, ApJ, 242, 359
Fletcher, L., & Hudson, H. S. 2008, ApJ, 675, 1645
Fletcher, L., & Martens, P. C. H. 1998, ApJ, 505, 418
Gary, D. E. 1996, in ASP Conf. Ser. 93, Radio Emission from the Stars and the Sun, ed. A. R. Taylor & J. M. Paredes (San Francisco, CA: ASP), 387
Grigis, P. C., & Benz, A. O. 2004, A&A, 426, 1093
Grigis, P. C., & Benz, A. O. 2008, ApJ, 683, 1180
Hamilton, R. J., & Petrosian, V. 1992, ApJ, 398, 350
Hanaoka, Y., et al. 1994, Proc. Kofu Symposium, New Look at the Sun with Emphasis on Advanced Observations of Coronal Dynamics and Flares, ed. S. Enome & T. Hirayama (Nagano: NAOJ), 35
Handy, B. N., et al. 1999, Sol. Phys., 187, 229
Hannah, I. G., Christe, S., Krucker, S., Hurford, G. J., Hudson, H. S., & Lin, R. P. 2008, ApJ, 677, 704
Howard, R. A., et al. 2008, Space Sci. Rev., 136, 67
Hoyng, P., et al. 1981, ApJ, 246, L155
Hudson, H. S. 1978, ApJ, 224, 235
Hudson, H. S. 2000, ApJ, 531, L75
Hurford, G. J., Schwartz, R. A., Krucker, S., Lin, R. P., Smith, D. M., & Vilmer, N. 2003, ApJ, 595, L77
Isobe, H., Yokoyama, T., Shimojo, M., Morimoto, T., Kozu, H., Eto, S., Narukage, N., & Shibata, K. 2002, ApJ, 566, 528
Ji, H., Huang, G., & Wang, H. 2007, ApJ, 660, 893
Kaiser, M. L., Kucera, T. A., Davila, J. M., St. Cyr, O. C., Guhathakurta, M., & Christian, E. 2008, Space Sci. Rev., 136, 5
Kontar, E. P., Dickson, E., & Kašparová, J. 2008, Sol. Phys., 252, 149
Kosugi, T., et al. 1991, Sol. Phys., 136, 17
Kosugi, T., et al. 2007, Sol. Phys., 243, 3
Krucker, S., Christe, S., Lin, R. P., Hurford, G. J., & Schwartz, R. A. 2002, Sol. Phys., 210, 445
Krucker, S., Hurford, G. J., & Lin, R. P. 2003, ApJ, 595, L103
Krucker, S., Hannah, I. G., & Lin, R. P. 2007, ApJ, 671, L193
Krucker, S., & Lin, R. P. 2002, Sol. Phys., 210, 229
Krucker, S., & Lin, R. P. 2008, ApJ, 673, 1181
Krucker, S., et al. 2008, A&ARv, 16, 115

Lin, R. P. 1974, Space Sci. Rev., 16, 189
Lin, R. P., et al. 2002, Sol. Phys., 210, 3
Liu, W., Jiang, Y. W., Liu, S., & Petrosian, V. 2004, ApJ, 611, L53
Liu, W., Petrosian, V., Dennis, B. R., & Jiang, Y. W. 2008, ApJ, 676, 704
Liu, Y., Luhmann, J. G., Bale, S. D., & Lin, R. P. 2009, ApJ, 691, L151
MacKinnon, A. L. 1985, Sol. Phys., 98, 293
Maetzler, C., Bai, T., Crannell, C. J., & Frost, K. J. 1978, ApJ, 223, 1058
Mariska, J. T., Sakao, T., & Bentley, R. D. 1996, ApJ, 459, 815
Masuda, S., Kosugi, T., Hara, H., Sakao, T., Shibata, K., & Tsuneta, S. 1995, PASJ, 47, 677
Masuda, S., Kosugi, T., Hara, H., Tsuneta, S., & Ogawara, Y. 1994, Nature, 371, 495
Masuda, S., Sato, J., Kosugi, T., & Sakao, T. 2000, Adv. Space Res., 26, 493
McKenzie, D. L. 1975, Sol. Phys., 40, 183
McKenzie, D. L., Datlowe, D. W., & Peterson, L. E. 1973, Sol. Phys., 28, 175
Miller, J. A., Larosa, T. N., & Moore, R. L. 1996, ApJ, 461, 445
Miller, J. A., et al. 1997, J. Geophys. Res., 102, 14631
Nakajima, H., et al. 1994, IEEE Proc., 82, 705
Petrosian, V., & Donaghy, T. Q. 1999, ApJ, 527, 945
Petrosian, V., Donaghy, T. Q., & McTiernan, J. M. 2002, ApJ, 569, 459
Petrosian, V., & Liu, S. 2004, ApJ, 610, 550
Ramaty, R. 1979, in AIP Conf. Ser. 56, Particle Acceleration Mechanisms in Astrophysics, ed. J. Arons, C. McKee, & C. Max (Melville, NY: AIP), 135
Roy, J.-R., & Datlowe, D. W. 1975, Sol. Phys., 40, 165
Saint-Hilaire, P., Krucker, S., & Lin, R. P. 2008, Sol. Phys., 250, 53
Schlemm, C. E., et al. 2007, Space Sci. Rev., 131, 393
Schmahl, E. J., Pernak, R. L., Hurford, G. J., Lee, J., & Bong, S. 2007, Sol. Phys., 240, 241
Smith, D. F., & Lilliequist, C. G. 1979, ApJ, 232, 582
Smith, D. M., et al. 2002, Sol. Phys., 210, 33
Somov, B. V., & Kosugi, T. 1997, ApJ, 485, 859
Sui, L., & Holman, G. D. 2003, ApJ, 596, L251
Sui, L., Holman, G. D., & Dennis, B. R. 2004, ApJ, 612, 546
Sui, L., Holman, G. D., & Dennis, B. R. 2005, ApJ, 626, 1102
Temmer, M., Veronig, A. M., Kontar, E. P., Krucker, S., & Vrsnak, B. 2010, ApJ, 712, 1410
Tomczak, M. 2001, A&A, 366, 294
Tomczak, M. 2009, A&A, 502, 665
Tsuneta, S., Masuda, S., Kosugi, T., & Sato, J. 1997, ApJ, 478, 787
Veronig, A. M., & Brown, J. C. 2004, ApJ, 603, L117
Veronig, A. M., Karlický, M., Vršnak, B., Temmer, M., Magdalenić, J., Dennis, B. R., Otruba, W., & Pötzi, W. 2006, A&A, 446, 675
Vlahos, L., & Papadopoulos, K. 1979, ApJ, 233, 717
Wheatland, M. S., & Melrose, D. B. 1995, Sol. Phys., 158, 283
Xu, Y., Emslie, A. G., & Hurford, G. J. 2008, ApJ, 673, 576
Zharkova, V. V., & Gordovskyy, M. 2006, ApJ, 651, 553